ADVANCED MATERIALS
www.advmat.de

Unlocking Multimodal Nonlinear Microscopy for Deep-Tissue Imaging under Continuous-Wave Excitation with Tunable Upconverting Nanoparticles

Jeongmo Kim, Seunghun Lee, Yundon Jeong, Kyunghwan Kim, Kibum Nam, Hyungwon Jin, Yuha Choi, Hyun-Jin Kim, Heungjin Ryu, Ki Hean Kim, Jae-Ick Kim, Jongnam Park, Jinmyoung Joo, and Jung-Hoon Park**

Nonlinear microscopy provides excellent depth penetration and axial sectioning for 3D imaging, yet widespread adoption is limited by reliance on expensive ultrafast pulsed lasers. This work circumvents such limitations by employing rare-earth doped upconverting nanoparticles (UCNPs), specifically Yb^{3+}/Tm^{3+} co-doped $NaYF_4$ nanocrystals, which exhibit strong multimodal nonlinear optical responses under continuous-wave (CW) excitation. These UCNPs emit multiple wavelengths at UV ($\lambda \approx 450$ nm), blue ($\lambda \approx 450$ nm), and NIR ($\lambda \approx 800$ nm), whose intensities are nonlinearly governed by excitation power. Exploiting these properties, multi-colored nonlinear emissions enable functional imaging of cerebral blood vessels in deep brain. Using a simple optical setup, high resolution in vivo 3D imaging of mouse cerebrovascular networks at depths up to 800 μmm is achieved, surpassing performance of conventional imaging methods using CW lasers. In vivo cerebrovascular flow dynamics is also visualized with wide-field video-rate imaging under low-powered CW excitation. Furthermore, UCNPs enable depth-selective, 3D-localized photo-modulation through turbid media, presenting spatiotemporally targeted light beacons. This innovative approach, leveraging UCNPs' intrinsic nonlinear optical characteristics, significantly advances multimodal nonlinear microscopy with CW lasers, opening new opportunities in bio-imaging, remote optogenetics, and photodynamic therapy.

1. Introduction

Advances in optical microscopy have enabled the observation of life in its native three-dimensional (3D) form.[1] However, 3D imaging does not come for granted and requires optical sectioning mechanisms which can differentiate information originating from different depths of the sample. This need has thus far been met by using techniques such as spatial, coherence, or nonlinear gating. Confocal microscopy, which employs spatial gating, has become a major workhorse in biomedical imaging as it can be built with a relatively simple optical setup and is readily realizable using common continuous-wave (CW) lasers. However, the penetration depth for high-resolution imaging using confocal microscopes is severely limited, typically under ≈100 μm for most biological tissues, due to the spatial gating pinhole and the relatively short excitation wavelengths for fluorescence excitation in the visible range which are both

J. Kim, S. Lee, Y. Jeong, K. Nam, H. Jin, Y. Choi, H. Ryu[+], J. Park, J. Joo, J.-H. Park
Department of Biomedical Engineering
Ulsan National Institute of Science and Technology (UNIST)
Ulsan 44919, Republic of Korea
E-mail: jjoo@unist.ac.kr; jh.park@unist.ac.kr

The ORCID identification number(s) for the author(s) of this article can be found under https://doi.org/10.1002/adma.202502739

[+]Present address: Graduate School of Informatics, Kyoto University, Kyoto, Kyoto 606-8501, Japan

DOI: 10.1002/adma.202502739

K. Kim
Department of Chemistry
Ulsan National Institute of Science and Technology (UNIST)
Ulsan 44919, Republic of Korea

H.-J. Kim, J.-I. Kim
Department of Biological Sciences
Ulsan National Institute of Science and Technology (UNIST)
Ulsan 44919, Republic of Korea

K. H. Kim
Division of Integrative Biosciences and Biotechnology
Pohang University of Science and Technology
77 Cheongam-Ro, Nam-gu, Pohang, Gyeongbuk 37673, Republic of Korea

J. Joo
Center for Genomic Integrity
Institute for Basic Science
Ulsan 44919, Republic of Korea

J. Joo
Graduate School of Health Science and Technology
Ulsan National Institute of Science and Technology (UNIST)
Ulsan 44919, Republic of Korea

vulnerable to multiple scattering in biological tissue. Optical coherence tomography (OCT), exploiting coherence gating, allows deeper imaging depths of around ≈1 mm by using longer wavelengths which suffer from less scattering and absorption. However, since coherence is required, this approach cannot be used for fluorescence imaging, which is crucial to obtain valuable molecular level contrast in many biological applications.

Nonlinear microscopy, on the other hand, does not require a pinhole or holographic measurements,[2] boasts deep penetration depths,[3] and is applicable to various fluorescent fluorophores.[4–6] Nonlinear microscopy has thus become the method of choice for fluorescence-based noninvasive 3D optical deep tissue imaging in the life sciences (e.g., tissue visualization, quantitative analysis, and neuroscience).[7–11] However, despite these advantages, the complexity and prohibitive cost of the excitation light source (ultrafast pulsed lasers) required for effective multiphoton absorption of fluorophores limit the wide applicability of nonlinear microscopy. Due to the low efficiency of the multi-photon absorption process, ultrafast pulsed lasers with very high peak powers in the range of MW cm^{-2} to GW cm^{-2} for two- and three-photon absorption is necessary.[12] Such intense laser irradiation poses other challenges such as photobleaching and phototoxicity, complicating prolonged monitoring of living specimens. Therefore, the current bottleneck in nonlinear microscopy, restricting its widespread use, is the requirement of high peak power in the excitation light source. In this regard, the development of CW laser-based nonlinear microscopy holds promise of overcoming these limitations, opening new avenues for broader applications by reducing costs and simplifying hardware requirements while taking advantages of nonlinear microscopy such as deep tissue imaging and photomodulation.

Considering the above, rare-earth doped upconverting nanoparticles (UCNPs) have been known to exhibit inherently strong nonlinear optical responses under CW laser excitation due to multistep excitation photon absorption, enabled by the presence of multiple real energy levels with extended lifetimes. This leads to the number of emitted photons to scale nonlinearly with respect to the excitation intensity.[13–19] We reasoned that this property can be optimally engineered to transform a typical laser scanning microscope into a highly nonlinear microscope equipped with 3D optical sectioning ability without using any pinholes or additional gating mechanisms. Moreover, this multistep absorption process of UCNPs is more efficient than the multiphoton absorption process relying on virtual energy levels as intermediate states.[5,20,21] For example, the popular green fluorescent protein has two- and three-photon absorption (2PA, 3PA) cross-sections of $\approx 10^{-49}$ cm^4 s/photon and $\approx 10^{-83}$ cm^6 (s/photon),^{2} respectively.[22–24] Due to this rapid drop in absorption probability, conventional multiphoton microscopes require ultrafast lasers with peak powers in the 100 kW to 10 MW range, which takes the bulk of the microscope cost as well as expertise. In stark contrast, our UCNPs sensitized with Yb^{3+} ions have a constant absorption cross section ($\approx 10^{-20}$ cm^2) regardless of the nonlinear emission. Due to this key difference, we can use the same laser source with peak power in the mW range to realize the entire scope of first-, second- and third-order nonlinear microscopy in a single setup. Recently, such unique optical properties of UCNPs have shown considerable promise for different purposes in enhancing resolution in various imaging modalities (e.g., emission saturation nanoscopy,[14,25] stimulated emission depletion microscopy,[26,27] sub-diffraction limited confocal microscopy,[17] and super-resolution nanoscopy[13,19,26]). However, the full extent of its optical sectioning and penetration capabilities in live animal imaging and the wide applicability to various nonlinearity-based applications remain unexplored, which we address in this study.

Furthermore, the multispectral emissions from UCNPs offer possibilities to enable multimodal functionalities in a single optical system. For example, the UCNPs used in this work ($NaYF_4$:Yb^{3+}/Tm^{3+}) exhibit emission bands at wavelengths ranging from NIR ($\lambda \approx 800$ nm), blue ($\lambda \approx 450$ nm), and UV ($\lambda \approx 350$ nm) under the excitation of a single NIR excitation beam ($\lambda \approx 976$ nm).[21,28,29] This is in stark contrast to conventional fluorophores that exhibit a broad emission spectrum with a single center peak. NIR emission is desirable for deep tissue imaging, which we targeted as the detection wavelength to enable wide-field (WF) imaging of brain blood flow. In comparison, the UV and blue emissions are of special interest in biomedical applications requiring photomodulation (e.g., biomolecular function regulation, optogenetics, drug release, and phototherapy).[30–32] The need for the delivery of light in photomodulation is especially interesting because UV and blue photons have the shortest penetration depth in tissue. Since the nonlinear optical property of the UCNPs allows for selective UV/blue photon generation at target depths using a deeply penetrating NIR excitation beam, photomodulation can be applied to specifically targeted 3D volumes in deep tissue with minimal phototoxicity to other non-targeted overlaying regions. This kind of targeted energy delivery is not feasible with fluorophores with a linear optical response since they emit photons across the entire excitation beam path and typically require excitation using short wavelengths in the blue/UV range which suffer from shorter scattering lengths.

In this study, we demonstrate the wide applicability of UCNPs-based nonlinear emissions to realize multimodal functionalities in a single optical platform. First, we explore the multiorder nonlinear optical response of the UCNPs upon variation of doping ratio, and demonstrate the spatially localized multicolor emission (UV/blue/NIR) of the UCNPs, followed by discussion on their effective 3D point-spread functions (PSFs). The UCNPs are then used for (i) high-resolution 3D imaging of mouse brain vasculature through opaque brain tissues reaching depths of d_{limit} ≈ 800 µm, (ii) investigation of in vivo subsurface cerebrovascular flow dynamics using WF video rate (30 fps) projection imaging, and (iii) generating depth-selective photomodulation light beacons at targeted volumetric foci in a localized 3D space through turbid media.

J. Joo
Materials Research Science and Engineering Center
University of California
San Diego, La Jolla, CA 92093, USA

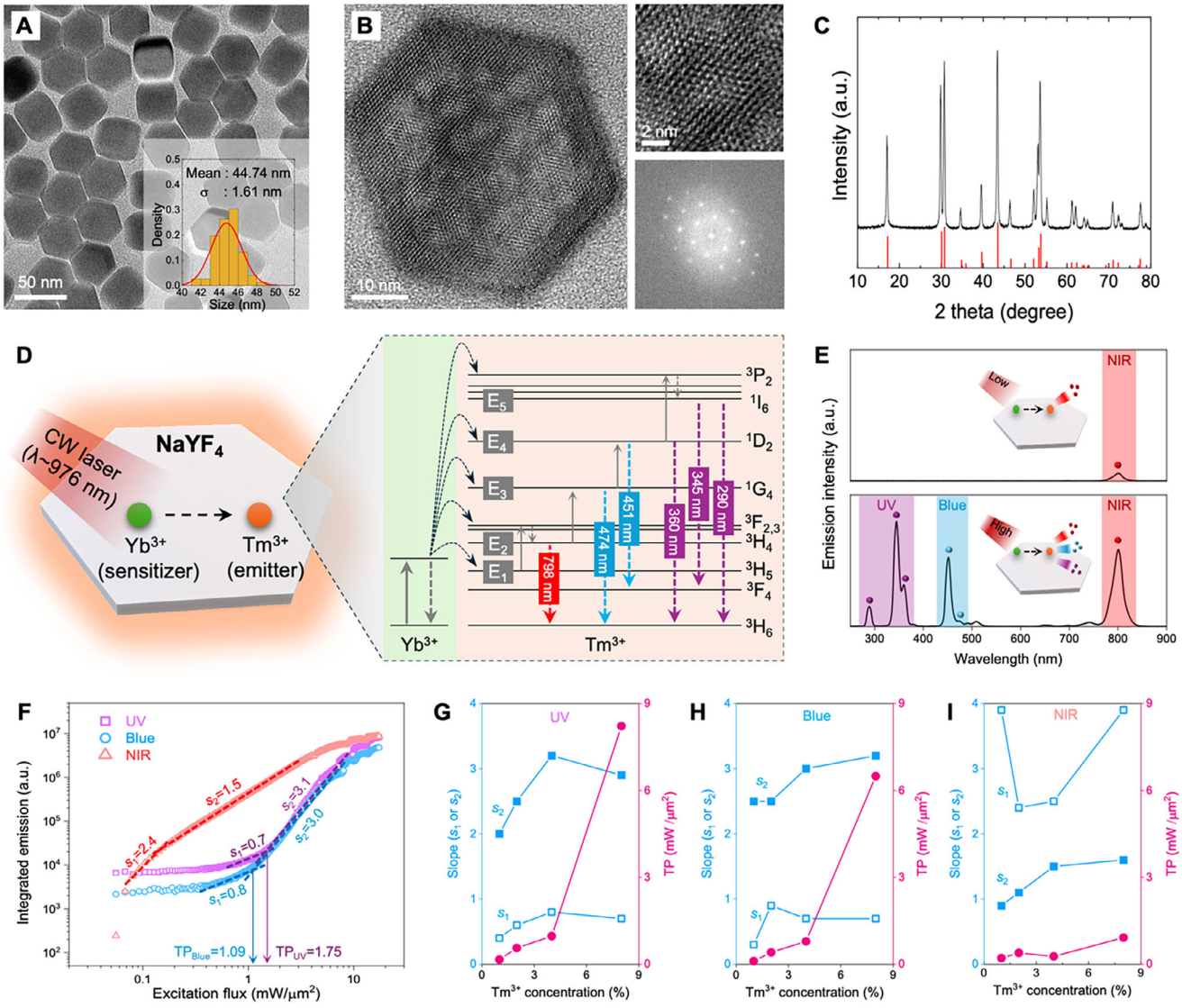

Figure 1. Nonlinear optical response of $NaYF_4$ crystals co-doped with Yb^{3+} and Tm^{3+} ions. A) Transmission electron microscopy (TEM) image and (inset) size distribution histogram of the UCNPs ($NaYF_4$:40%Yb^{3+}/4%Tm^{3+}). B) High-resolution TEM images with fast Fourier transformation (FFT) of the UCNPs. C) X-ray diffraction (XRD) pattern of UCNPs. Reference XRD pattern of hexagonal β-$NaYF_4$ (JCPDS 16-0334) is displayed in red line. D) Schematic illustration depicting energy levels and transfer in the nanocrystals co-doped with Yb^{3+} sensitizing ions and Tm^{3+} emitting ions. E_n (n = 1, 2, 3, 4, 5) indicates the n-photon excited state. E) Emission spectra of UCNPs ensemble dispersed in cyclohexane under CW laser irradiation (λ_{ex}: 976 nm) at excitation flux of ≈0.7 mW μm^{-2}, acquisition time ≈1 s (top) and ≈49.5 mW μm^{-2}, acquisition time ≈1/20 s (bottom), respectively. F) Integrated emission intensity of UCNPs ensemble at different wavelength ranges (UV/blue/NIR) as a function of excitation flux. The value s indicates the slope of the log-log plot ($I_{emission} \propto I_{excitation}^{s}$). Threshold power (TP) indicates excitation flux where the slope (s) abruptly changes from sub-linear ($s_1 < 1$) to super-linear ($s_2 > 1$) for blue and UV emissions. G–I) The slopes (s_1 and s_2) and TP values of each emission band indicate nonlinear transition of optical response upon variation of Tm^{3+} doping ratio, obtained from (F) and Figure S3 (Supporting Information). Note that the lines are connected between the scatter points to guide the eye.

2. Results

2.1. Nonlinear Optical Responses of UCNPs

The UCNPs used in this work comprises a high concentration of 40% Yb^{3+} (sensitizer) and 4% Tm^{3+} (emitter) doped in $NaYF_4$ host crystal. The $NaYF_4$ nanocrystals, co-doped with Yb^{3+}/Tm^{3+}, were synthesized via hot injection of organometallic precursors to produce homogeneous nuclei at elevated temperature. As-synthesized UCNPs display hexagonal symmetry with an average diameter of 45 nm and high crystallinity (**Figure** 1A–C). The UCNPs exhibit a photon upconversion process that sequentially absorbs multiple low-energy photons in a step-like manner and emits higher-energy photons[16] (Figure 1D). We designed the UCNPs such that the sensitizing ions (Yb^{3+}) absorb NIR photons ($\lambda \approx 976$ nm) and nonradiatively transfer the absorbed energy to the emitting ions (Tm^{3+}). Due to long lifetime of the excited states at Tm^{3+}, the series of stepwise

excitation to the higher energy levels ($E_1 \rightarrow E_5$) resulted in multiple emission bands at shorter wavelengths: UVB ($\lambda \approx 290$ nm), UVA ($\lambda \approx 345$ and 360 nm), blue ($\lambda \approx 451$ and 474 nm), and NIR ($\lambda \approx 798$ nm). This upconverting multistep absorption process incorporates rich energy-distribution mechanisms, including excited-state absorption, energy transfer upconversion, ground-state absorption, nonradiative relaxation, cross-relaxation, energy-looping, and photon-avalanche.[13,15,19,26,33–38] These mechanisms, coupled with the long lifetimes of intermediate excited states, result in inherently strong nonlinear optical responses, leading to a transition from suppressed emission to lasing emission in UCNPs.[13,17,19,39,40]

To leverage the multi-order nonlinear optical responses, we first examined the emission spectra of the UCNPs pumped with a CW laser ($\lambda \approx 976$ nm) at various excitation fluxes. Interestingly, at lower excitation flux (<1 mW μm^{-2}), as the excitation flux increases, the rise in emission intensity from the E_2 [$\lambda \approx 798$ nm ($^3H_4 \rightarrow {}^3H_6$)] is dominant, while the emission intensities from the higher excited states (E_3, E_4, and E_5) increases only slightly and remain relatively very low in intensity (Figure 1E and Figure S1, Supporting Information). This result emphasizes that the light irradiation contributes mostly to the photon population at E_2, thereby increasing the NIR ($\lambda \approx 798$ nm) emission intensity upon elevated excitation flux (Figure S1A, Supporting Information). In contrast, at higher excitation flux (>1 mW μm^{-2}), higher-photon excited states (E_3, E_4, and E_5) are effectively populated, resulting in occurrence of emission bands at the UV and blue wavelengths. Notably, the transition from E_3 [$\lambda \approx 474$ nm ($^1G_4 \rightarrow {}^3H_6$)], E_4 [$\lambda \approx 451$ nm ($^1D_2 \rightarrow {}^3F_4$) and $\lambda \approx 360$ nm ($^1D_2 \rightarrow {}^3H_6$)] and E_5 [$\lambda \approx 345$ nm ($^1I_6 \rightarrow {}^3F_4$) and $\lambda \approx 290$ nm ($^1I_6 \rightarrow {}^3H_6$)] becomes more dominant (Figure S1B, Supporting Information). In addition, the higher-photon excited states (E_3, E_4, and E_5) are much favorably populated than lower-photon excited states (E_2), resulting in dominant emissions in the shorter wavelengths upon irradiation with higher excitation flux.

In light of this finding, we then compared the integrated emission intensity of each band (UV, blue, and NIR) with incremental excitation flux scanning to reveal a threshold power (TP) responsible for the nonlinear optical characteristics (Figure 1F and Figure S2, Supporting Information). At low excitation flux, the slope (s_1) of the log–log plot ($I_{emission} \propto I_{excitation}{}^s$) is super-linear for NIR photons ($s_1 \approx 2.5$) while sub-linear for UV ($s_1 \approx 0.7$) and blue photons ($s_1 \approx 0.8$), emphasizing that the emission from the higher-photon excited states (E_3, E_4, and E_5) is suppressed presumably due to the insufficient excitation power. However, at a certain TP of excitation flux, the slope (s_2) for UV and blue photons shifts abruptly from sub-linear (<1) to super-linear (>1) regimes. For instance, the s_2 increases to ≈3.1 and 3.0 for UV and blue, respectively, above TP. This nonlinearity is the key to realize the sub-diffraction limited resolution and 3D deep tissue imaging using CW excitation, as well as depth-selective photomodulation. In addition, the contrasting emission properties observed in the NIR and UV/blue emissions (opposite inversion of s_1 and s_2 as a function of incident flux) are most probably attributed to the differing photon states that controls the emission energy pathway.[17,25,41] We exploit this unique characteristic of lanthanide ions as the basis for the dual-modality capability, enabling both 3D deep-tissue imaging and 2D wide-field real-time imaging with a CW excitation and same optical setup (further discussed in Sections 2.3 and 2.4).

The nonlinear optical response of our UCNPs can be modulated by varying the doping contents of emitting Tm^{3+} ions (Figure 1G–I and Figures S3–S5, Supporting Information), and the tunability is eligible to optimize the UCNPs for tailored imaging applications. Although the size of UCNPs varies slightly with the doping amount of Tm^{3+}, such minor size differences do not significantly alter the multiphoton absorption processes or energy transfer mechanisms that govern the nonlinear luminescence.[42,43] Instead, the optical properties are primarily dictated by the Tm^{3+} doping concentration, which directly affects the population dynamics of the intermediate energy levels and energy transfer efficiency among sensitizer and activator ions. For both UV and blue emissions, the TP increases with higher Tm^{3+} doping contents, possibly due to the cross-relaxation process preventing the higher-photon state from being activated.[33,34] The highest s_2 value above TP was found at 4% and 8% of Tm^{3+} doping for UV and blue emission, respectively. While nanocrystals with the lowest s_1 and the highest s_2 are desirable for achieving a sharper 3D emission localization, we used $NaYF_4$:40%Yb^{3+}/4%Tm^{3+} for the following studies as 8% Tm^{3+} doping requires comparably high TP which is not desirable for bioimaging, and high s_1 for NIR emission of 8% Tm^{3+} doped UCNPs may potentially reduce photon conversion to UV or blue emission. Furthermore, the sufficiently high NIR emission intensity and higher nonlinearity at low excitation flux enables WF imaging. In-depth investigations on the expected 3D optical imaging performance, in connection with the tunability of UCNPs, are further discussed in Note S1 (Supporting Information).

2.2. 3D Diffraction Limited Fluorescence Localization

Exploiting the nonlinear optical response of UCNPs with thresholding behavior, we next investigated the 3D sub-diffraction limited fluorescence localization. Considering the Gaussian distribution of excitation beam intensity as a function of distance from the focal plane, the UV and blue emissions of UCNPs show a transition where the slope (s) of emission upon elevated excitation flux jumps from sub-linear (s_1) to super-linear (s_2) at the boundary energy defined by TP (**Figure 2A**). This implies that the UCNPs emit few photons at out-of-focus planes (sub-linear, excitation flux below TP, blue line in Figure 2A) while the emission intensity increases nonlinearly as a function of the excitation flux raised to the power of s (≈3 for blue and ≈3.1 for UV) near the focal plane (super-linear, excitation flux above TP, red line in Figure 2A). Therefore, the full width at half maximum (FWHM) of the emission point spread functions (PSF) can be smaller than the FWHM of the diffraction limit of the excitation beam.

We directly confirmed 3D confinement of UCNPs emissions under focused light excitation (Figure 2B). The UCNPs were filled in a cuvette, and the CW excitation beam (λ: 976 nm) was focused using an objective lens (NA = 0.3) to the center of the cuvette. The resulting emissions of the UCNPs were spectrally filtered using bandpass filters (λ_{UV}: 325–375 nm; λ_{blue}: 450–490 nm; λ_{NIR}: 705–845 nm) placed in front of the camera. We found all emissions to be spatially localized at the

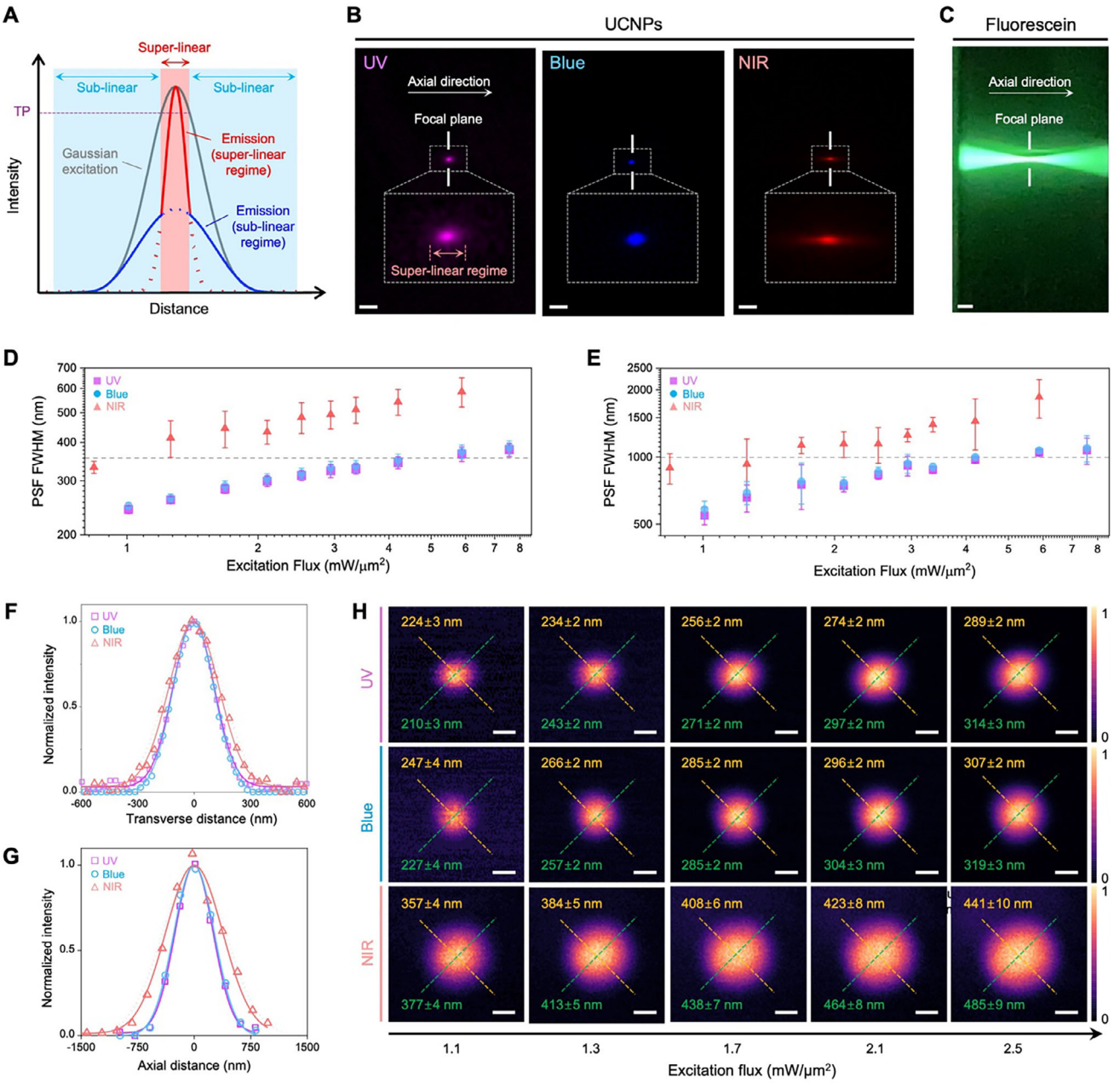

Figure 2. Spatially localized fluorescence and increased resolution by the nonlinear optical response of the UCNPs. A) A conceptual diagram of sub-diffraction limited 3D localized fluorescence. TP indicates threshold power. The gray line shows a Gaussian excitation intensity distribution of which is higher than TP near the focal plane and lower away from the focal plane. The solid blue and red lines illustrate UCNPs emission intensities for the sub-linear and super-linear regimes, respectively. B) Fluorescence images of the UCNPs filled in a cuvette under a focused CW excitation beam (λ: 976 nm). The multi-colored emissions from UCNPs (UV/blue/NIR) are selectively filtered using bandpass filters. The images within dotted square show the zoom-in of emissions. Scale bar: 1 mm. C) Fluorescence image of fluorescein filled in a cuvette under a focused CW excitation beam (λ: 488 nm). A green emission filter was used to filter out the blue excitation laser. Scale bar: 1 mm. The measured PSF FWHM of UCNPs emission per different wavelength ranges (UV/blue/NIR) as a function of excitation flux along the D) transverse and E) axial directions. Scatter points and error bar indicate the mean value and the standard deviation, respectively ($N \geq 3$). Gray horizontal lines indicate the theoretically calculated FWHM of the diffraction limit. Normalized intensity profiles of each emission band (scatter points), Gaussian fitted line, and theoretically calculated diffraction-limited Gaussian distribution (black dotted line) for F) transverse and G) axial directions (UV/blue: ≈1.3 mW μm^{-2}, NIR: ≈0.8 mW μm^{-2}). H) Fluorescence images of single UCNP measured along transverse direction at different excitation fluxes. The measured PSF FWHM for two diagonal linecuts are noted in the image. Scale bar: 200 nm.

focal plane where the excitation flux was highly concentrated. The NIR emission at the focal plane is relatively more elongated than the UV and blue emissions due to its relatively lower degree of nonlinearity. Thus, simply changing the position of a CW laser focus enables the emission to appear exclusively at the arbitrarily selectable focal spot within a continuous 3D volume (Video S1, Supporting Information). In comparison, the green emission of fluorescein under a focused CW excitation beam (λ: 488 nm) was distributed following the conical shape of the focused excitation beam path (Figure 2C), which is typically observed for linear fluorescent emitters. In this case, optical sectioning can only be realized by resorting to multiphoton absorption with high-peak power pulsed-lasers or adding confocal gating. However, the nonlinear optical response of our UCNPs opens the possibility of spatially controllable excitation and emission characteristics with low power CW light irradiation.

To validate the sub-diffraction limited 3D confinement, we next measured the transverse and axial PSFs at each emission band. The UCNPs were uniformly deposited on a coverslip by spin coating, and the excitation beam was focused on single UCNPs using an oil immersion objective (NA = 1.4). The CW laser focus scanning optical setup was used for single nanoparticle imaging (Figure S6A,C, Supporting Information). The PSFs at each emission band showed the dependence on their distinct nonlinearity at various excitation fluxes (Figure 2D,E). Conventional fluorophores have a single absorption cross section per nonlinear excitation process, implying s to be only 2 or 3 for two- or three-photon microscopy, respectively. However, our UCNPs exhibit varying s values at a series of excitation fluxes, emphasizing controllable PSF FWHM by simply adjusting excitation flux. Notably, the PSF FWHM increases for both transverse and axial directions when the excitation flux increases. At the lowest excitation flux when the measurable emission intensities rise above the noise floor, the transverse PSF FWHM from each emission band of UCNPs was 242 ± 7 nm (UV), 249 ± 6 nm (blue), and 332 ± 15 nm (NIR), while the axial PSF FWHM was 547 ± 50 nm (UV), 584 ± 49 nm (blue), and 895 ± 139 nm (NIR), respectively. It should be noted that the theoretical PSF FWHM of transverse ($0.51 \cdot \lambda/\mathrm{NA}$) and axial ($2 \cdot \lambda/\mathrm{NA}^2$) diffraction limits for the given optical configuration and excitation wavelength are 356 and 996 nm, respectively.[44] Comparing to theoretical values, the sharpest measured values of transverse PSF FWHM are enhanced by a factor of $\approx\sqrt{2.2}$, $\approx \sqrt{2.1}$, and $\approx \sqrt{1.1}$ and the axial PSF FWHM are enhanced by a factor of $\approx \sqrt{3.3}$, $\approx \sqrt{2.9}$, and $\approx \sqrt{1.2}$ for the UV, blue, and NIR emission, respectively. Normalized intensity profiles for transverse and axial directions compared with the theoretical diffraction-limited PSF confirm the sub-diffraction PSF FWHM (Figure 2F,G). Transverse PSF imaging of a single UCNP at various excitation flux shows enhanced PSF FWHM accordingly (Figure 2H). We also performed numerical simulations of the PSF, assuming the ideal case where there are no aberrations throughout the entire optical system. In this ideal case, the transverse PSF FHWM can be enhanced by a factor of $\approx \sqrt{3.2}$, $\approx \sqrt{3.1}$, and $\approx \sqrt{1.8}$ for the UV, blue, and NIR emission, respectively (Figure S7, Supporting Information). Although the enhancement factors found in experiments were slightly smaller than those of theoretically expected values, further optimization of the optics by utilizing adaptive optics to reduce system aberrations will improve the sub-diffraction limit and 3D confinement.[45–47]

2.3. High-Resolution 3D Deep Tissue Imaging Using UCNPs and CW Laser Excitation

We next investigated the effective optical sectioning and penetration capabilities of 3D fluorescence imaging using UCNPs under CW laser irradiation. The inherent nonlinear optical property of our UCNPs enables optical depth sectioning simply by focusing the scanned laser beam in a straightforward CW laser-based laser scanning microscope (**Figure 3A**; Figure S6A,C, Supporting Information). Among the various emissions from UCNPs, we used the blue emission as it shows higher s_2 value than NIR and undergoes less scattering than UV. In addition, photomultiplier tubes, which are often used as a detector for laser scanning microscopes, exhibit the highest quantum efficiency in the visible range.

Adjusting the excitation flux for each depth to obtain optimal PSF and signal-to-noise ratio (SNR) (see the Experimental Section), we acquired fluorescence images of live mouse cerebrovascular networks at various depths in vivo (Figure 3B). These images exhibit a distinct spatial distribution of vascular networks, confirming the axial sectioning power provided by the inherent nonlinear optical characteristics of UCNPs. The high-absorption cross-section and high-order nonlinearity of the UCNPs enabled achieving a FWHM of ≈0.9 µm (Figure 3C) and a signal-to-background ratio (SBR) of ≈10.0 (Figure 3D) at a depth up to 850 µm in the opaque brain tissue. It is important to note that deep tissue imaging is fundamentally limited by the SBR since it is the out of focus fluorescence (background) that overwhelms the wanted signal as the target focal plane gets deeper.

Subsequently, we compared the penetration depth limit of our technique with other state-of-the-art methods. Utilizing our UCNPs-based nonlinear microscopy (Figure 3E), we visualized live mouse cerebrovascular structures up to depths beyond ≈800 µm through opaque brain tissues. This underscores the feasibility of achieving in vivo 3D fluorescence live imaging in deep tissues through CW laser excitation. In comparison, a 2-photon microscope (2PM) using a femtosecond pulsed laser (λ: 920 nm, Figure S8, Supporting Information) could visualize fluorescein-dextran dye injected vessels up to a similar penetration depth limit of ≈800 µm (Figure 3F). We would like to emphasize that comparable imaging depths and imaging quality were obtained using readily accessible CW laser excitation which is less costly than the pulsed lasers required for nonlinear excitation of fluorophores by 2–3 orders of magnitude. In stark contrast, confocal microscopy which is the current gold standard to obtain depth selective imaging using CW laser excitation was restricted to imaging up to only about 100 µm depths in live mouse brain (Figure 3G). This limitation is expected, as the confocal pinhole blocks most of the scattered fluorescence emission, while CW excitation at a shorter wavelength is also more susceptible to scattering. The depth sectioned images using UCNPs-based nonlinear microscopy, 2PM, and confocal microscopy are directly compared in Video S2 (Supporting Information).

We further compared the SBR in the deep regions between our UCNPs-based nonlinear microscopy and 2PM [Figure 3B(iii),H].

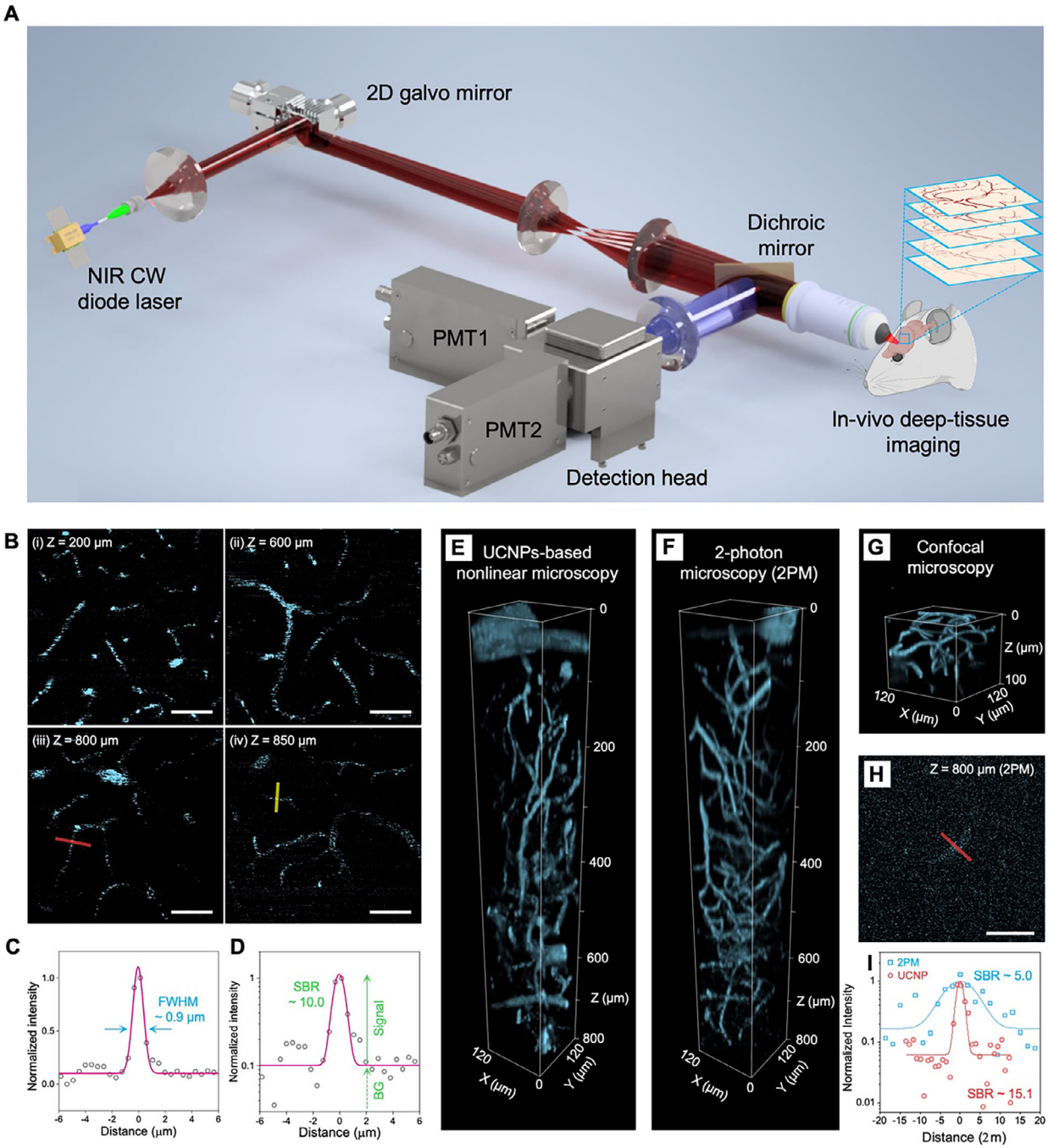

Figure 3. Three-dimensional in vivo fluorescence imaging of mouse cerebrovascular. A) Schematic diagram of the laser-scanning optical setup with a focused illumination for 3D deep tissue imaging. PMT = Photomultiplier tube. B) Fluorescence images of in vivo mouse cerebrovascular networks injected with UCNPs obtained at different depths (Z = 200, 600, 800, and 850 µm from the brain surface). The UCNPs are excited with a NIR CW laser (λ_{ex}: 976 nm), and the emission is filtered using a blue bandpass filter (λ: 450–490 nm). Pixel dwell time = 100 µs. Averaging factor = 5. Scale bar = 50 µm. Intensity scatter points of the yellow linecut indicated in B(iv) and its Gaussian-fitted line (solid line), showing C) FWHM of ≈0.9 µm and D) signal-to-background ratio (SBR) of ≈10.0. E) 3D-rendered fluorescence image of UCNPs-injected in vivo mouse cerebrovascular network. Pixel dwell time = 100 µs. No averaging. F) 3D-rendered fluorescence image of two-photon microscopy (2PM) of fluorescein-dextran-injected in vivo mouse cerebrovascular network. The dye is excited with a femtosecond pulsed laser (λ: 920 nm), and the emission is filtered using a green bandpass filter (λ: 490–560 nm). Pixel dwell time = 88 ns. Averaging factor = 8. G) 3D-rendered fluorescence image of confocal microscopy of Lectin-FSD488-stained ex vivo mouse brain vasculature. The dye is excited with a CW excitation source (λ: 473 nm), and the resulting emission is filtered through a pinhole (1 airy unit) and a green bandpass filter (λ: 485–585 nm). Pixel dwell time = 8 µs. No averaging. H) Fluorescence image of fluorescein-dextran-injected in vivo mouse cerebrovascular network obtained at the depth of 800 µm from the brain surface using 2PM. I) Intensity scatter points of the red linecut indicated in (B(iii) and H) and its Gaussian-fitted line (red and blue solid line for UCNPs and 2PM, respectively), showing SBR of ≈5.0 for 2PM and ≈15.1 for UCNP-based nonlinear microscopy.

It should be highlighted that threefold higher SBR (≈15.1) was achieved in UCNPs-based nonlinear microscopy than the 2PM (≈5.0) at the same depth (800 μm from the brain surface) (Figure 3I). While the 2PM image could only visualize larger vessels with low SBR, the UCNPs-based imaging showed not only these vessels but also capillary-sized vessels in the deeper region. We attribute this favorable imaging characteristic to the high nonlinearity and optical thresholding behavior within the nonlinear optical response of UCNPs, where emission is suppressed for sub-threshold excitation at the lower intensity boundaries of the distorted PSF at deeper regions (see Note S1, Supporting Information, for more discussions). In comparison, the resolution and axial PSF confinement for conventional 2PM degrades as a function of depth due to aberrations and scattering from the overlaying tissues.[48]

Based on these results, we believe that the use of affordable CW excitation, while enabling deep tissue penetration, is poised to bring new possibilities in optical imaging technology. In addition, the UCNPs-based 3D imaging substantially alleviates many requirements in the optical setup that can potentially bring deep tissue 3D imaging into the reach of a broader community. For example, none of the following is needed: a confocal pinhole and de-scanning of emitted fluorescence (confocal microscopy), an ultrafast pulsed laser (multiphoton microscopy), or a reference arm/interferometric stability and broadband excitation source (optical coherence tomography).

2.4. Wide-Field Video-Rate Optical Imaging

Since the UCNPs have a high absorption cross-section, it is also possible to readily perform high-speed WF imaging using the same probe and optical setup under identical excitation light irradiation. Simply converting the mode of excitation light illumination from focused to WF facilitates a seamless transition from 3D nonlinear imaging to 2D volumetric projection WF imaging (Figure S6, Supporting Information). Experimentally, transitioning the light illumination mode from focused to WF requires only the removal of a scan lens that is mounted on a detachable magnetic stage while keeping the rest of optical setup and sample exactly in the same condition. In the focused illumination mode, the PMTs were used to obtain the emission signals from the focal plane, while a CMOS camera was adopted to collect the emission signals upon collimated plane wave illumination after removing the scan lens in the WF mode. Notably, we should also highlight that in traditional nonlinear microscopy using conventional fluorophores and pulsed lasers, a single excitation source or optical setup typically cannot be used for both focused and WF excitation. Since the nonlinear absorption cross-sections of conventional fluorophores are orders of magnitude smaller than their linear absorption counterparts, it leads to excitation efficiency becoming almost negligible for WF excitation which requires even higher peak powers only obtainable by employing additional amplifiers.

To enable WF imaging beyond superficial tissue layers, we chose to measure the NIR emission peak ($\lambda \approx 800$ nm) as the longer wavelength is more penetrating and shows higher emission intensity at low excitation flux. Using a low magnification, moderate resolution objective lens (10×, NA = 0.3) to simultaneously visualize vessels at various depths in a large field of view, we observed vascular structures up to around 200-μm-thick volumes in single-shot WF measurements at video rate (30 fps), benefiting from the reduced scattering in NIR for both excitation and emission upon administration of UCNPs (**Figure** 4A and Video S3, Supporting Information). The results clearly showed the cerebral vasculatures of varying diameters at different depths and their interconnections in mouse brain. The intensity profile of a thin vessel exhibited micron-scale resolution via WF video-rate optical imaging, which emphasizes highly favorable, fast extended depth imaging capability with UCNPs and WF illumination (Figure 4B,C).

The WF video-rate imaging further works for the investigation of flow dynamics. Although individual UCNPs were not visualized in this configuration due to limited resolution, dynamic flow of the UCNPs in the blood vessels were clearly recognizable (Video S3, Supporting Information). In addition, certain UCNP aggregates, possibly derived by protein corona formation on the nanoparticle surface, were much brighter than monomeric UCNPs, thereby allowing the displacement tracking in a given exposure time (1/30 s) to visualize microvascular flow rate (Figure 4D). The fluidic velocity of each aggregate in mouse brain vasculatures was found to range from 0.5 to 11 mm s^{-1}, in accordance with the literature.[49] In addition, rapid fluidic movement of the aggregates was found in the proximal region rather than near the vascular wall, possibly due to shear stress at the vascular rim (Figure 4E,F). It should also be noted that the UCNPs tend to flow faster in larger vessels. Overall, the rapid WF imaging capability of UCNPs allows studying dynamic transport in cerebral vasculature. The direct applicability of UCNPs for both focused (Figure 3) and WF excitation modalities (Figure 4) is another important feature that can broaden the utilization range of UCNP-based nonlinear microscopy.

2.5. Depth-Selective Photomodulation

Finally, we propose the use of efficient UV emission from UCNPs under CW laser excitation for depth-selective photomodulation. UV photons are common excitation sources in a variety of photomodulation applications, including optogenetics,[50] on-demand drug release, nanomanufacturing, and photodynamic therapy.[30–32,51–54] However, UV photons have the shortest penetration depth due to their severe scattering and strong absorption in biological tissue. As a result, effective delivery of UV photons into deeper layers of biological tissue poses a challenge, limiting targeted photomodulation primarily to superficial layers. This is one of the main reasons UCNPs, which convert less-scattering NIR photons into UV photons, have been widely used, particularly in neuromodulation applications. However, in the case of UCNPs with low nonlinearity, when applying NIR irradiation, the excitation affects the entire overlying volume along the light beam path, including all UCNPs within this volume, making depth-selective photomodulation unachievable.

To overcome these issues, we suggest the use of the UCNPs with a high nonlinearity as a secondary UV excitation source inside deep tissue. As discussed, our UCNPs can provide localized fluorescence within a small 3D volume, thereby providing the depth-selective photomodulation capability for various

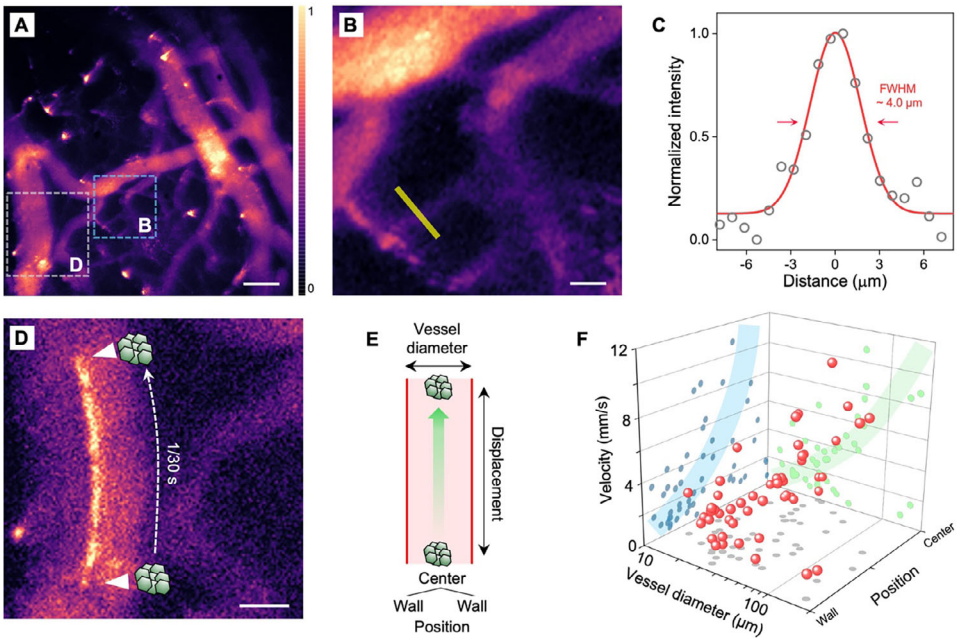

Figure 4. In vivo wide-field real-time imaging of mouse brain vasculature. A) Averaged intensity of fluorescence images of UCNPs-injected, in vivo mouse brain vasculature taken at different time frames, using a NIR CW wide-field illumination and an uncooled industrial CMOS camera. The UCNPs are excited with a CW excitation source (λ: 976 nm), and the emission is filtered using an NIR bandpass filter (λ: 705–845 nm). Scale bar: 50 μm. B) Magnified image of the blue dotted square region in A. Scale bar: 10 μm. C) Intensity profile of the linecut indicated by the yellow line in B and its Gaussian-fitted line (red solid line) showing a FWHM of ≈4.0 μm. D) A single image frame taken from the source video (30 fps) at the gray dotted square region in (A). White arrow heads indicate the start and end positions of a UCNP aggregate displaced during one time frame (1/30 s). Scale bar: 20 μm. E) A schematic illustration showing the analysis model to calculate the flow velocity of UCNPs aggregates depending on the vessel diameter and the position of flow. F) Calculated velocity (red spheres) of UCNPs aggregates flowing through blood vessels per vessel diameter and the position. Green dots are the projection showing velocity per vessel diameter, and blue dots are the projection showing velocity per position.

applications that use UV photons for excitation (**Figure** 5A and Table S1, Supporting Information). Spectral responses of various photomodulating agents (e.g., photo-responsive proteins, photocurable resin, photoresist, photosensitizers, and fluorescent dyes) are eligible to utilize the UCNPs as a UV excitation source in depth-selective manner.[53]

As a proof of concept, we demonstrated 3D depth-selective excitation using UCNPs (excitation beacon), achieving 3D-localized emission of fluorescent dyes (photomodulable reservoir). Mixed aqueous solution of Hoechst 33342 and UCNPs in a quartz cuvette was prepared and irradiated by either UV (λ: 365 nm) or NIR (λ: 976 nm). Hoechst 33342 is an organic fluorescent dye with a broad excitation band in the UV range ($\lambda_{peak} \approx 350$ nm) that overlaps with the UV emission from the UCNPs ($\lambda \approx 350$ nm), enabling UCNPs to operate as a feasible light source at a 3D confined location (Figure 5B). Under direct excitation of Hoechst 33342 via a focused UV excitation beam, the fluorescence emerges along the entire excitation beam, following the conical shape of the excitation beam path (Figure 5D). In contrast, selective UV emission of UCNPs under NIR irradiation at the focal plane leads to localized excitation of Hoechst 33342 only in the confined volume, emphasizing the capability of UCNPs to enable depth-selective photomodulation (Figure 5E). The photomodulation process proceeds through (1) the excitation of UCNPs by CW NIR light, (2) 3D-localized UV emission from UCNPs, (3) 3D-localized excitation of Hoechst 33342, and (4) 3D-localized emission of the fluorescent Hoechst 33342. Based on the prompt photon transfer from the UCNPs to the molecular dye at the localized volume, a variety of photomodulation applications utilizing UCNPs as excitation beacons will be pursued in future studies.

In addition to depth selectivity, the UCNPs-based 3D localized excitation is also beneficial for higher penetration depth while overcoming substantial light scattering in turbid environment. The external excitation light has to penetrate through densely packed tissues for in vivo applications. A scattering tissue phantom layer was thus placed deliberately in front of the cuvette to investigate the effect of light scattering (Figure 5C). The degree of optical scattering in the tissue phantom layer was controlled by varying the mass concentration (C_m) of polystyrene beads mixed in water and agarose (Table S2, Supporting Information). The UV excitation beam undergoes severe scattering and becomes completely diffused at moderate degrees of turbidity corresponding to brain tissue thickness of ≈50 μm (Figure 5D and Table S2, Supporting Information). On the other hand, the less-scattering NIR excitation beam for the UCNPs maintains its focus, and the resulting Hoechst 33342 emission at the focal spot is still clearly visible even up to strong levels of turbidity corresponding to brain tissue thickness of 550 μm (Figure 5E and Table S2, Supporting Information). Subsequently, we repeated the experiment without the bandpass filter in optically opaque situations (Figure S9, Supporting Information). In this case, we observed clear emission signals of UCNPs only at the focal spot for even stronger scattering corresponding to brain tissue thickness of 980 μm.

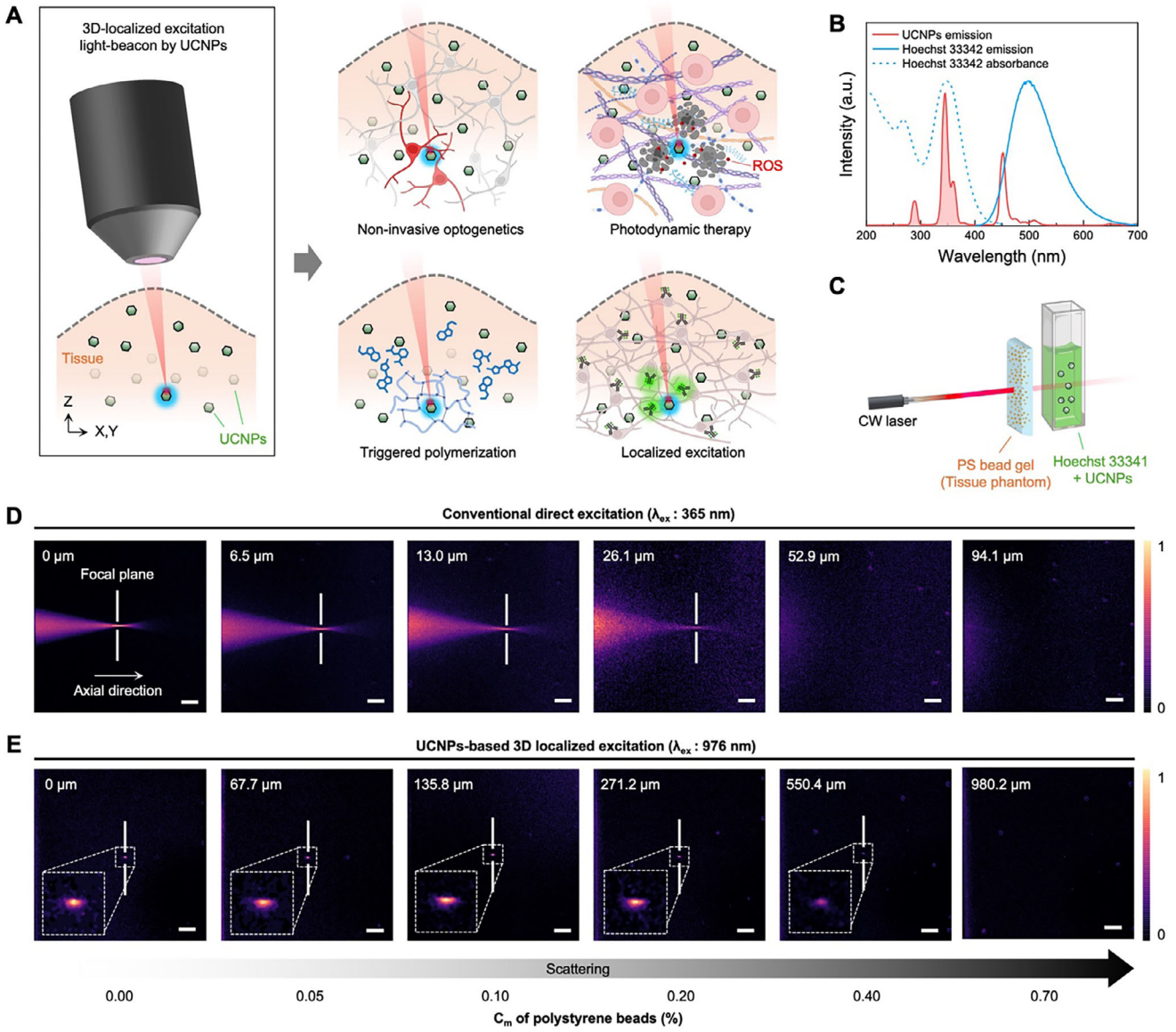

Figure 5. Generation of 3D localized excitation light-beacon for depth-selective photomodulation. A) Schematic illustrations of depth-selective photomodulating applications using the 3D localized UV emission from the UCNPs. B) Emission spectra of UCNPs (red solid line, λ_{ex}: 976 nm) and Hoechst 33342 (blue solid line, λ_{ex}: 350 nm) with an absorbance spectrum of Hoechst 33342 (blue dotted line) dispersed in water. Red-colored area indicates the cross-section between UCNPs emission and Hoechst 33342 absorbance. C) A schematic diagram illustrating the measurement of 3D localized excitation and emission capability. D,E) Fluorescence images of Hoechst 33342 and UCNPs mixed aqueous solution filled in a cuvette. The same sample was excited with a focused excitation beam of two different wavelengths (λ: 365 or 976 nm). A bandpass filter (λ: 570–640 nm) was placed in front of the camera to selectively capture the emission from Hoechst 33342. To demonstrate the spatially localized excitation of Hoechst 33342 by UCNPs-based light-beacon via deep tissue-penetrable NIR, the tissue phantom layer is placed in front of the excitation beam path. The degree of light scattering was controlled by varying the mass concentration (C_m) of polystyrene beads embedded in the mixture of water and agarose. Theoretically calculated corresponding brain tissue thicknesses are noted in the images. Scale bar: 1 mm.

This implies that the depth limit of indirect excitation using UCNPs can be further improved by optimizing energy transfer. In summary, we demonstrated that the use of UCNPs as an indirect excitation source provides depth-selective photomodulation with enhanced tissue penetration compared to direct UV excitation which can be potentially used as a general means that can be extended to various biomedical applications (Figure 5A).

3. Discussions

We achieved high-resolution in vivo 3D imaging of mouse cerebrovascular structure up to 850 μm in the opaque brain tissue using a simple CW laser scanning microscope system, rivaling the high-resolution deep tissue imaging performance of 2PM driven by much more costly ultrafast pulsed lasers. Moreover, the high absorption cross-section of the UCNPs facilitated seamless

transition from 3D imaging to 2D WF imaging using the same optical setup, probe, and excitation source by simply adjusting the setup from focused to WF illumination mode. The video-rate WF imaging enabled the exploration of in vivo blood flow dynamics across extensive deep brain volumes, utilizing simultaneous NIR excitation and emission wavelengths. Beyond imaging capabilities, we also unveiled the potential of UCNPs emission as secondary 3D localized light beacons for depth-selective photomodulation. Deep tissue penetration was generically obtained based on the NIR excitation, while the 3D localized UV emission could be utilized for depth-selective photomodulation applications, showing their promise in developing new strategies to deliver energy to specific highly resolved targeted depths without affecting overlaying volumes. Although many studies have reported the UCNPs as a light beacon using deep tissue penetrable NIR excitation for fluorescent probes that require shorter wavelength excitation, this work reports the first depth-selective emission of UCNPs that utilize the nonlinear optical response under CW light irradiation, to the best of our knowledge.

It should be noted that we observed a transition in slope behavior for NIR emission under CW excitation, with a higher slope ($s_1 = 2.5$) at low excitation flux and a reduced slope ($s_2 = 1.5$) at higher flux, consistent with nonlinear upconversion dynamics. The slope transition is influenced by excited-state saturation, ground-state depletion, and energy transfer quenching mechanisms, which are well-established in the literature for both nanoparticles and common fluorescent molecules.[13,19,55,56] However, more importantly, at a specific TP of excitation flux, we also observed an abrupt transition in the slope for UV and blue emissions from sub-linear ($s_1 < 1$) to super-linear ($s_2 > 1$) regimes. This inversion in slope magnitudes represents a key feature of the multimodal nonlinear microscopy explored in this study, while NIR emission shows higher s_1 and lower s_2 aligned with previously observed phenomena in upconverting nanoparticles.[17,25,41] These findings represent significant progress toward low-cost 3D deep-tissue imaging and photomodulation applications. Although this work provides a clear experimental framework, additional investigation involving computational simulations would offer further insight into the complex energy redistribution mechanisms for nanoparticle design.

Looking forward, there remains ample opportunity for improving the performance of applications based on the UCNPs. First, remarkable advancements have been recently made in utilizing UCNPs to achieve exceptionally high orders of nonlinearity (with s_2 reaching ≈46), promising substantial enhancements in imaging performance, particularly in 3D resolution.[13,18,19] For bio-imaging applications that require penetration of thick scattering layers by both excitation and emitted photons, achieving the highest nonlinearity may not be the key factor. For 3D imaging, it is crucial to address the loss in excitation and emission intensity at greater depths, as well as the corresponding decrease in absolute emission intensity caused by overly small PSFs due to very high nonlinearity. Another aspect that we must consider is the fact that higher nonlinearity in UCNPs results in increased fluorescence rise/decay lifetimes (a few hundreds of ms and µs for rise and decay times) which makes 3D large volume imaging of live animals practically impossible.[13] These factors underscore the necessity of optimizing the balance between nonlinearity (resolution) and the absolute excitation versus emission intensity.

Second, exploring the nonlinear optical properties of alternative UCNPs design could further enhance the intrinsic 3D bio-imaging applications without the need for additional depth-gating mechanisms, as demonstrated in this study. For example, replacing Yb^{3+} ($\lambda_{ex} \approx 976$ nm) with Nd^{3+} ($\lambda_{ex} \approx 808$ nm) as a sensitizer could be considered to minimize heating effects, which are commonly associated with longer excitation wavelengths.[57] Another promising strategy involves incorporating Yb^{3+}-doped $NaYF_4$ shell layer instead of a bare $NaYF_4$ shell to further enhance upconversion luminescence by improving energy transfer efficiency and mitigating surface quenching. In addition, utilizing the downshifted emission lines from lanthanide-doped nanoparticles presents an interesting opportunity for deeper tissue penetration. Emission wavelengths in the infrared range (e.g., 1185 nm for Ho^{3+}, 1310 nm for Pr^{3+}, 1475 nm for Tm^{3+}, 1525 nm for Er^{3+}) experience significantly reduced tissue scattering compared to the visible wavelengths, potentially allowing for increased penetration depths. Investigating the nonlinearity of these nanoparticles could contribute to the development of an emission nonlinearity library, which would serve as a valuable resource for advancing intrinsic 3D bio-imaging applications without reliance on external gating mechanisms.

Third, optimizing the kinetics of rise and decay times in the UCNPs also holds potential for increasing scanning imaging speed. In our measurements, we observed emission rise times of a few milliseconds, with decay times ranging from tens to hundreds of microseconds (Figure S10, Supporting Information). These timescales are indeed longer when compared to the nano- or pico-second ranges typical of organic fluorophores. Consequently, a tradeoff exists between imaging speed and the amount of collected emission intensity. Further discussions about 3D optical sectioning ability and its related scanning imaging speed are made in Figure S11 and Note S2 (Supporting Information). In this context, recent developments regarding UCNPs' emission lifetime engineering, such as the incorporation of a plasmonic cavity,[58] present promising avenues.

We have also observed that the UCNPs may aggregate when they are immersed for extended periods in highly ionic liquids. This underscores the need for additional surface functionalization chemistries to improve the colloidal stability, potentially employing substances like zwitterionic polymer[59] or dendrimers.[60,61] Furthermore, it is worth noting that modifying UCNPs' surface with protein binding ligands (e.g., lectin) could facilitate direct utilization of UNCPs for various bio-sample preparation techniques.[62,63] Leveraging our current imaging platform, we can investigate the real-time dynamics of ligand-functionalized UCNPs and quantify their targeting efficiency under different physiological conditions. In addition, optimizing nanoparticle size, surface charge, and ligand density could further improve brain-targeting efficacy while maintaining the intrinsic nonlinear optical properties of UCNPs. Such advancements would broaden the application of UCNPs in neuroscience research, enabling deeper insights into neurovascular function and pathology.

The importance of observing life in their 3D native environment has become increasingly evident.[7,64] In this respect, nonlinear microscopy has risen to be the method of choice for many applications in noninvasive deep tissue 3D imaging due to the deep penetration depth and high contrast. Despite the relatively

straightforward optical configuration of 2PM, which is even simpler than a confocal microscope, easy adoption has been hindered by the cost and physical volume of ultrafast femtosecond lasers. These factors which require investments greater than CW lasers by several orders of magnitude have limited the deployment of multi-photon microscopes only to well-funded specialized labs and imaging centers. Considering that the excitation source is currently the biggest barrier, we believe that the presented study will drive further research to optimize the optical response of UCNPs to bring the benefits of nonlinear microscopy to the broader scientific community.

Our study presents a significant advancement in the field of bioimaging and photomodulation by leveraging the intrinsic high nonlinearity of UCNPs to achieve true 3D imaging and spatially confined light delivery using CW lasers. Unlike conventional imaging approaches that rely on additional confocal gating or volumetric projections, our method enables simultaneous 2D and 3D visualization without added system complexity. This capability is particularly advantageous for applications requiring precise depth selectivity, such as deep-tissue neuroimaging and targeted photomodulation. Furthermore, the ability of our UCNPs to generate UV and blue emissions strictly within the focal volume opens new possibilities for noninvasive neuromodulation and optogenetics in live biological systems. By addressing key challenges associated with current imaging techniques and introducing a versatile, low-power alternative, our work paves the way for future innovations in minimally invasive biomedical applications.

4. Conclusion

In this study, we demonstrated NIR CW excitation-based multimodal nonlinear microscopy by exploiting the nonlinear optical response of UCNPs co-doped with Yb^{3+} and Tm^{3+} ions. High-resolution in vivo 3D imaging of mouse cerebrovascular structures in opaque brain tissue was achieved using a CW laser scanning microscope system, in which high absorption cross-section of the UCNPs allowed a seamless switching from 3D to 2D wide-field imaging, enabling detailed exploration of blood flow dynamics across extensive deep brain volumes with the same setup. In addition, UCNPs served as 3D localized light beacons for depth-selective photomodulation, providing a novel method for targeted energy delivery. This work reports the first depth-selective emission of UCNPs utilizing the nonlinear optical response under CW light irradiation. While commonly benefiting from the deep penetration depth of NIR excitation, the multispectral emission from our UCNPs ranging across the UV, blue, and NIR ranges enabled a variety of biomedical applications utilizing sub-diffraction limited resolution and inherent optical depth sectioning.

Supporting Information

Supporting Information is available from the Wiley Online Library or from the author.

Acknowledgements

This work was supported by the National Research Foundation of Korea (2019M3E5D2A01063812, 2021R1A2C3012903, 2021R1A4A1031644, RS-2023-00264980), the Ministry of Science and ICT (IITP-2023-RS-2023-00259676), the Korea Dementia Research Center (KDRC) funded by the Ministry of Health & Welfare and Ministry of Science and ICT (RS-2020-KH106391), the Korean Fund for Regenerative Medicine (KFRM) grant (22A0102L1-11) funded by the Korea government (the Ministry of Science and ICT, the Ministry of Health & Welfare), the Korea Basic Science Institute (National Research Facilities and Equipment Center) grant funded by the Korea government (RS-2024-00403508), and the TJ Park Foundation. This work was also supported in part by National Science Foundation (NSF) through the UC San Diego Materials Research Science and Engineering Center (UCSD MRSEC) DMR-2011924. The authors thank UNIST Central Research Facilities (UCRF) and UNIST Optical Biomedimaging Center (UOBC) for the support of its facilities and equipment. The authors acknowledge Prof. C. Y. Lee for the kind help on spectroscopic measurements. All animal experimental procedures were conducted in accordance with protocols approved by the Institutional Animal Care and Utilization Committee of UNIST (UNISTIACUC-22-37).

Conflict of Interest

The authors declare no conflict of interest.

Author Contributions

J.K. and S.L. contributed equally to this work. J.K. and J.-H.P. developed the idea, designed the project, and wrote the original manuscript with input from all authors. J.K., Y.C., J.P., and J.J. developed the synthesis and surface chemistry of the UCNPs. J.K., K.K., and J.J. prepared the spectroscopic characterization system. J.K. and K.N. performed simulations. J.K., S.L., K.K., H.-J.K., H.R., and J.-I.K. prepared animal experiments. J.K., S.L., Y.J., K.N., K.H.K., and J.-H.P. prepared the optical imaging setup. H.J. prepared the scattering layer. J.K., S.L., Y.J., and K.N. conducted the imaging experiments. J.J. and J.-H.P. supervised the research.

Data Availability Statement

The data that support the findings of this study are available in the supplementary material of this article.

Keywords

continuous-wave excitation, deep-tissue imaging, multimodal imaging, nonlinear microscopy, upconverting nanoparticle

Received: February 10, 2025
Published online: March 21, 2025

[1] J. G. Fujimoto, D. Farkas, *Biomedical Optical Imaging*, Oxford University Press, Oxford **2009**.
[2] P. T. C. So, C. Y. Dong, B. R. Masters, K. M. Berland, *Annu. Rev. Biomed. Eng.* **2000**, *2*, 399.
[3] P. G. Bush, D. L. Wokosin, A. C. Hall, *Front. Biosci.* **2007**, *12*, 2646.
[4] C. Xu, R. M. Williams, W. Zipfel, W. W. Webb, *Bioimaging* **1996**, *4*, 198.
[5] G. S. He, L.-S. Tan, Q. Zheng, P. N. Prasad, *Chem. Rev.* **2008**, *108*, 1245.
[6] D. R. Larson, W. R. Zipfel, R. M. Williams, S. W. Clark, M. P. Bruchez, F. W. Wise, W. W. Webb, *Science* **2003**, *300*, 1434.
[7] W. R. Zipfel, R. M. Williams, W. W. Webb, *Nat. Biotechnol.* **2003**, *21*, 1369.

[8] W. Denk, K. Svoboda, *Neuron* **1997**, *18*, 351.
[9] J. H. Park, L. Kong, Y. Zhou, M. Cui, *Nat. Methods* **2017**, *14*, 581.
[10] S. You, H. Tu, E. J. Chaney, Y. Sun, Y. Zhao, A. J. Bower, Y. Z. Liu, M. Marjanovic, S. Sinha, Y. Pu, S. A. Boppart, *Nat. Commun.* **2018**, *9*, 2125.
[11] Y. S. Jin, D. Kim, H. Roh, S. Kim, S. Hussain, J. Y. Kang, C. G. Pack, J. K. Kim, S. J. Myung, E. Ruoslahti, M. J. Sailor, S. C. Kim, J. Joo, *Adv. Mater.* **2018**, *30*, 18002878.
[12] K. Konig, *J. Microsc.* **2000**, *200*, 83.
[13] C. Lee, E. Z. Xu, Y. Liu, A. Teitelboim, K. Yao, A. Fernandez-Bravo, A. M. Kotulska, S. H. Nam, Y. D. Suh, A. Bednarkiewicz, B. E. Cohen, E. M. Chan, P. J. Schuck, *Nature* **2021**, *589*, 230.
[14] C. Chen, B. Liu, Y. Liu, J. Liao, X. Shan, F. Wang, D. Jin, *Adv. Mater.* **2021**, *33*, 2008847.
[15] M. Pollnau, D. R. Gamelin, S. R. Lüthi, H. U. Güdel, M. P. Hehlen, *Phys. Rev. B* **2000**, *61*, 3337.
[16] G. Chen, C. Yang, P. N. Prasad, *Acc. Chem. Res.* **2013**, *46*, 1474.
[17] D. Denkova, M. Ploschner, M. Das, L. M. Parker, X. Zheng, Y. Lu, A. Orth, N. H. Packer, J. A. Piper, *Nat. Commun.* **2019**, *10*, 3695.
[18] C. Chen, D. Jin, *Nat. Photonics* **2022**, *16*, 553.
[19] Y. Liang, Z. Zhu, S. Qiao, X. Guo, R. Pu, H. Tang, H. Liu, H. Dong, T. Peng, L.-D. Sun, J. Widengren, Q. Zhan, *Nat. Nanotechnol.* **2022**, *17*, 524.
[20] G. Chen, H. Ågren, T. Y. Ohulchanskyy, P. N. Prasad, *Chem. Soc. Rev.* **2015**, *44*, 1680.
[21] F. Auzel, *Chem. Rev.* **2004**, *104*, 139.
[22] L. D. DeLoach, S. A. Payne, L. L. Chase, L. K. Smith, W. L. Kway, W. F. Krupke, *IEEE J. Quantum Electron.* **1993**, *29*, 1179.
[23] L.-C. Cheng, N. G. Horton, K. Wang, S.-J. Chen, C. Xu, *Biomed. Opt. Express* **2014**, *5*, 3427.
[24] C. Xu, W. W. Webb, in *Topics in Fluorescence Spectroscopy: Nonlinear and Two-Photon-Induced Fluorescence*, Vol. *5*, (Ed: J. R. Lakowicz), Springer US, Boston, MA **2002**.
[25] C. Chen, F. Wang, S. Wen, Q. P. Su, M. C. L. Wu, Y. Liu, B. Wang, D. Li, X. Shan, M. Kianinia, I. Aharonovich, M. Toth, S. P. Jackson, P. Xi, D. Jin, *Nat. Commun.* **2018**, *9*, 3290.
[26] Y. Liu, Y. Lu, X. Yang, X. Zheng, S. Wen, F. Wang, X. Vidal, J. Zhao, D. Liu, Z. Zhou, C. Ma, J. Zhou, J. A. Piper, P. Xi, D. Jin, *Nature* **2017**, *543*, 229.
[27] L. Liang, Z. Feng, Q. Zhang, T. D. Cong, Y. Wang, X. Qin, Z. Yi, M. J. Y. Ang, L. Zhou, H. Feng, B. Xing, M. Gu, X. Li, X. Liu, *Nat. Nanotechnol.* **2021**, *16*, 975.
[28] F. Wang, X. Liu, *Chem. Soc. Rev.* **2009**, *38*, 976.
[29] G. Chen, H. Qiu, P. N. Prasad, X. Chen, *Chem. Rev.* **2014**, *114*, 5161.
[30] V. W. Karisma, W. Wu, M. Lei, H. Liu, M. F. Nisar, M. D. Lloyd, C. Pourzand, J. L. Zhong, *Front. Cell Dev. Biol.* **2021**, *9*, 598717.
[31] R. Tong, H. D. Hemmati, R. Langer, D. S. Kohane, *J. Am. Chem. Soc.* **2012**, *134*, 8848.
[32] A. Losi, K. H. Gardner, A. Möglich, *Chem. Rev.* **2018**, *118*, 10659.
[33] W. Wei, Y. Zhang, R. Chen, J. Goggi, N. Ren, L. Huang, K. K. Bhakoo, H. Sun, T. T. Y. Tan, *Chem. Mater.* **2014**, *26*, 5183.
[34] A. Baride, P. S. May, M. T. Berry, *J. Phys. Chem. C* **2020**, *124*, 2193.
[35] E. S. Levy, C. A. Tajon, T. S. Bischof, J. Iafrati, A. Fernandez-Bravo, D. J. Garfield, M. Chamanzar, M. M. Maharbiz, V. S. Sohal, P. J. Schuck, B. E. Cohen, E. M. Chan, *ACS Nano* **2016**, *10*, 8423.
[36] B. Tian, A. Fernandez-Bravo, H. Najafiaghdam, N. A. Torquato, M. V. P. Altoe, A. Teitelboim, C. A. Tajon, Y. Tian, N. J. Borys, E. S. Barnard, M. Anwar, E. M. Chan, P. J. Schuck, B. E. Cohen, *Nat. Commun.* **2018**, *9*, 3082.
[37] G. Wang, W. Qin, L. Wang, G. Wei, P. Zhu, R. Kim, *Opt. Express* **2008**, *16*, 11907.
[38] Q. Liu, Y. Zhang, C. S. Peng, T. Yang, L. M. Joubert, S. Chu, *Nat. Photonics* **2018**, *12*, 548.
[39] A. Fernandez-Bravo, K. Yao, E. S. Barnard, N. J. Borys, E. S. Levy, B. Tian, C. A. Tajon, L. Moretti, M. V. Altoe, S. Aloni, K. Beketayev, F. Scotognella, B. E. Cohen, E. M. Chan, P. J. Schuck, *Nat. Nanotechnol.* **2018**, *13*, 572.
[40] H. Li, X. Wang, D. Huang, G. Chen, *Nanotechnology* **2019**, *31*, 072001.
[41] J. Kim, H. S. Park, Y. Ahn, Y. J. Cho, H. H. Shin, K. S. Hong, S. H. Nam, *ACS Nano* **2023**, *17*, 648.
[42] S. Wilhelm, *ACS Nano* **2017**, *11*, 10644.
[43] B. Zhou, B. Tang, C. Zhang, C. Qin, Z. Gu, Y. Ma, T. Zhai, J. Yao, *Nat. Commun.* **2020**, *11*, 1174.
[44] T. Latychevskaia, *Appl. Opt.* **2019**, *58*, 3597.
[45] C. Ahn, B. Hwang, K. Nam, H. Jin, T. Woo, J.-H. Park, *J. Innov. Opt. Health Sci.* **2019**, *12*, 1930002.
[46] H. Jin, B. Hwang, S. Lee, J.-H. Park, *Optica* **2021**, *8*, 428.
[47] M. J. Booth, *Light: Sci. Appl.* **2014**, *3*, e165.
[48] R. Niesner, V. Andresen, J. Neumann, H. Spiecker, M. Gunzer, *Biophys. J.* **2007**, *93*, 2519.
[49] G. Meng, J. Zhong, Q. Zhang, J. S. J. Wong, J. Wu, K. K. Tsia, N. Ji, *Proc. Natl. Acad. Sci. USA* **2022**, *119*, 2117346119.
[50] A. H. All, X. Zeng, D. B. L. Teh, Z. Yi, A. Prasad, T. Ishizuka, N. Thakor, Y. Hiromu, X. Liu, *Adv. Mater.* **2019**, *31*, 1803474.
[51] S. Chen, A. Z. Weitemier, X. Zeng, L. He, X. Wang, Y. Tao, A. J. Y. Huang, Y. Hashimotodani, M. Kano, H. Iwasaki, L. K. Parajuli, S. Okabe, D. B. L. Teh, A. H. All, I. Tsutsui-Kimura, K. F. Tanaka, X. Liu, T. J. McHugh, *Science* **2018**, *359*, 679.
[52] X. Wang, M. Jiang, Z. Zhou, J. Gou, D. Hui, *Composites, Part B* **2017**, *110*, 442.
[53] H.-L. Wei, W. Zheng, X. Zhang, H. Suo, B. Chen, Y. Wang, F. Wang, *Adv. Opt. Mater.* **2023**, *11*, 2201716.
[54] M. Lan, S. Zhao, W. Liu, C.-S. Lee, W. Zhang, P. Wang, *Adv. Healthcare Mater.* **2019**, *8*, 1900132.
[55] X. Yin, W. Xu, G. Zhu, Y. Ji, Q. Xiao, X. Dong, M. He, B. Cao, N. Zhou, X. Luo, L. Guo, B. Dong, *Nat. Commun.* **2022**, *13*, 6549.
[56] L. Ding, C. Chen, X. Shan, B. Liu, D. Wang, Z. Du, G. Zhao, Q. P. Su, Y. Yang, B. Halkon, T. T. Tran, J. Liao, I. Aharonovich, M. Zhang, F. Cheng, L. Fu, X. Xu, F. Wang, *Adv. Mater.* **2024**, *36*, 2308844.
[57] L. M. Wiesholler, F. Frenzel, B. Grauel, C. Wurth, U. Resch-Genger, T. Hirsch, *Nanoscale* **2019**, *11*, 13440.
[58] H. Chen, Z. Jiang, H. Hu, B. Kang, B. Zhang, X. Mi, L. Guo, C. Zhang, J. Li, J. Lu, L. Yan, Z. Fu, Z. Zhang, H. Zheng, H. Xu, *Nat. Photonics* **2022**, *16*, 651.
[59] Z. Wang, F. Delille, S. Bartier, T. Pons, N. Lequeux, B. Louis, J. Kim, T. Gacoin, *Langmuir* **2022**, *38*, 10512.
[60] S. Plunkett, M. El Khatib, İ. Şencan, J. E. Porter, A. T. N. Kumar, J. E. Collins, S. Sakadžić, S. A. Vinogradov, *Nanoscale* **2020**, *12*, 2657.
[61] T. V. Esipova, X. Ye, J. E. Collins, S. Sakadžić, E. T. Mandeville, C. B. Murray, S. A. Vinogradov, *Proc. Natl. Acad. Sci. USA* **2012**, *109*, 20826.
[62] M. Ghanimi Fard, Z. Khabir, P. Reineck, N. M. Cordina, H. Abe, T. Ohshima, S. Dalal, B. C. Gibson, N. H. Packer, L. M. Parker, *Nanoscale Adv.* **2022**, *4*, 1551.
[63] J. Wang, D. Liu, Z. Wang, *Anal. Methods* **2011**, *3*, 1745.
[64] C. Jensen, Y. Teng, *Front. Mol. Biosci.* **2020**, *7*.